Ball milling effects for induced carriers and reduced grain size on thermoelectric properties in $Bi_{1-x}Sr_xCuSeO$ $(x = 0, 0.1)$

2016 Jpn. J. Appl. Phys. 55 115801

(http://iopscience.iop.org/1347-4065/55/11/115801)

Japanese Journal of Applied Physics **55**, 115801 (2016)
http://doi.org/10.7567/JJAP.55.115801

REGULAR PAPER

Ball milling effects for induced carriers and reduced grain size on thermoelectric properties in $Bi_{1-x}Sr_xCuSeO$ ($x = 0, 0.1$)

Shu Mizuno[1], Mamoru Ishizawa[1], Hiroyuki Fujishiro[1]*, Tomoyuki Naito[1], Hirokazu Katsui[2], and Takashi Goto[2]

[1]*Faculty of Science and Engineering, Iwate University, Morioka 020-8551, Japan*
[2]*Institute for Materials Research, Tohoku University, Sendai 980-8577, Japan*

*E-mail: fujishiro@iwate-u.ac.jp

Received May 24, 2016; revised July 23, 2016; accepted July 30, 2016; published online October 5, 2016

We have investigated the ball milling effects for thermoelectric $Bi_{1-x}Sr_xCuSeO$ ($x = 0, 0.1$) materials. The characteristic rotation speed R for the ball milling exists, at which the crystallite size of the starting powder suddenly decreased. The grain size in the bulks sintered using ball-milled powders also decreased and thermoelectric properties were enhanced mainly by the induced carriers, rather than by the reduction in thermal conductivity. The ball milling effects of carrier doping on thermoelectricity are discussed. © 2016 The Japan Society of Applied Physics

1. Introduction

The thermoelectric technology using waste heat for power generation devices has been revived because of the recent energy crisis together with other renewable energy sources. The performance of thermoelectric materials can be written using the dimensionless figure of merit, ZT ($= S^2T/\rho\kappa$), and the power factor P ($= S^2/\rho$), where S is the Seebeck coefficient, T is the absolute temperature, ρ is the electrical resistivity, and κ is the thermal conductivity. Most conventional thermoelectric bulk materials with high ZT values, such as Bi_2Te_3 and PbTe, exhibit thermal and chemical instabilities in air at elevated temperatures, and contain toxic, scarce or expensive elements.[1–3] Nevertheless, oxide materials could be potential candidates in thermoelectric applications on the basis of their advantages over heavy metallic alloys in terms of chemical and thermal robustness, although the present potential is relatively low.

Typical n-type thermoelectric oxides are $SrTi_{0.8}Nb_{0.2}O_3$ ($ZT = 0.37$ at 1000 K),[4] $Zn_{0.98}Al_{0.02}O$ ($ZT = 0.30$ at 1273 K),[5] $In_{2-x}Ge_xO_3$ ($ZT = 0.45$ at 1273 K),[6] and so forth. On the other hand, typical p-type thermoelectric oxides are mainly layered cobaltites: Ti-doped $Ca_3Co_4O_9$ ($ZT = 0.3$ at 1000 K),[7] Na_xCoO_2 ($ZT = 0.8$ at 1050 K),[8] and so forth, in which relatively higher Seebeck coefficients and lower thermal conductivities are realized using the layered structure. However, it is necessary to explore high-performance thermoelectric oxide polycrystals for practical applications.

Recently, oxyselenides, BiCuSeO, have been paid considerable attention for a relatively higher thermoelectric performance from 700 to 1000 K.[9–21] This material crystallizes in a layered crystal structure that is composed of conductive $[Cu_2Se_2]^{2-}$ layers constituting a conduction pathway for carrier transport alternately stacked with insulating $[Bi_2O_2]^{2+}$ layers acting as a charge reservoir along the c-axis of the tetragonal unit cell, which is similar to layered cobaltites and iron-based superconductors.[10,11] The main features of the BiCuSeO system can be summarized as follows: a moderate effective mass ($m^* \sim 0.6m_0$), a low hole mobility (2–20 $cm^2\,V^{-1}\,s^{-1}$) and a relatively high carrier concentration ($n \sim 10^{18}\,cm^{-3}$).[17] The thermal conductivity κ is low ($= 4.6$ $mW\,cm^{-1}\,K^{-1}$ at 873 K),[16] resulting from a large Gruneisen parameter ($\gamma \sim 1.5$) and a low Young's modulus ($E \sim 76.5$ GPa).[21] The presence of Bi, which is a heavy element and is known to exhibit strong anharmonic vibrations, is also detrimental for heat transfer. To enhance the thermoelectric properties, BiCuSeO showed an excellent charge transport behavior owing to the introduction of hole carriers by replacing Bi^{3+} with divalent alkaline-earth ions such as Sr^{2+}, Ba^{2+}, Ca^{2+}, and Pb^{2+} in the insulating $[Bi_2O_2]^{2+}$ layer.[16,17,21] In the $[Cu_2Se_2]^{2-}$ layer, the replacement of the Se^{2-} site with the isovalent Te^{2-} for the opening of a small gap in the electronic structure[22] and the deficiency of Cu^+[23] were also investigated by the introduction of hole carriers. Hole doping also induces point defect scattering, which reduces the thermal conductivity. The highest ZT of 1.4 was achieved at 923 K for the $Bi_{0.875}Ba_{0.125}CuSeO$ sample to date.[24]

A ball milling technique is widely used to pulverize powder finely before spark plasma sintering (SPS) to reduce the thermal conductivity of bulk materials. For the pristine BiCuSeO compound, Li et al. fabricated bulk samples by SPS using BiCuSeO powders ball-milled at 250 rpm for various milling times from 0 to 1500 min. They investigated the thermoelectric properties of the sintered bulks,[25] in which ZT was increased mainly by increasing the electrical conductivity. Pele et al. investigated the milling time (80–600 min) and rotation speed (400–800 rpm) dependences of BiCuSeO powders by mechanical alloying (MA) and, subsequently, the bulk samples were fabricated by SPS using powders under different MA conditions,[26] in which the optimum MA condition exists for the starting powders. The ball milling procedure, at the same time, introduces a deficiency of the metal element and oxygen, and also creates an amorphous phase. These crystal defects introduce electron or hole carriers to the crystallites and subsequently sintered bulks, which are supposed to affect the electrical and thermoelectric properties. However, the ball milling effect on the crystallite size and the relationship between the initial crystallite size and the subsequent grain size of the sintered bulk fabricated by SPS have not been clarified systematically so far. Also, the mechanism of the charge carrier creation has not been investigated in detail.

In this study, we performed the ball milling procedure for the nondoped and Sr-doped $Bi_{1-x}Sr_xCuSeO$ ($x = 0, 0.1$) powders under various rotation speeds (R), in which we selected Sr as a dopant for the Bi site. Because Sr is a popular dopant in divalent alkaline-earth ions, we investigated the effects of ball milling on the crystallographic and thermoelectric properties of the $Bi_{1-x}Sr_xCuSeO$ system.

2. Experimental procedure

To fabricate $Bi_{1-x}Sr_xCuSeO$ ($x = 0, 0.1$) materials, Bi (99.9%) and Bi_2O_3 (99.9%), SrO (99.5%), Cu (99.9%), Se (99.9%), and SrO (99.5%) fine powders were used as raw materials. These were weighed with a stoichiometoric ratio of Bi : Sr : Cu : Se = $1 - x : x : 1 : 1$ and mixed in Ar atmosphere. After the mixed raw materials were evacuated and sealed in a quartz tube, they were heated at 973 K for 12 h and then furnace-cooled. The obtained precursor was pulverized and mixed in air for 0.5 h using an automatic mortar. The $Bi_{1-x}Sr_xCuSeO$ powder obtained at this stage was named the "0 rpm" powder. Using this powder, four types of $Bi_{1-x}Sr_x$-CuSeO starting powders of about 9 g were ball-milled using a planetary ball milling apparatus (Retsch PM100) for 6 h with 25 stainless steel (SUS304) balls (0.95 cm in diameter) and a vial (77 cm^3) under the rotation speed R from 100 to 400 rpm. The volume ratio of the powder to balls in the vial is about 1 : 11. The apparatus was stopped for 1 min every 1 h and counter-rotated for milling effectively. These ball-milled powders were named "$R = 100$ rpm" to "$R = 400$ rpm". The powders were sintered using the SPS apparatus (NJS LABOX-110C) under a uniaxial pressure of 40 MPa at about 973 K for 10 min in vacuum. The mass density of the obtained pellets (10 mm in diameter and 9 mm in thickness) was higher than 93% of the ideal density.

Powder X-ray diffraction (XRD) measurements were performed (Rigaku Multi Flex) at room temperature using Cu Kα radiation to estimate the crystallite size of the starting powder using the Scherrer equation,[27] and to confirm the impurity phase in the starting powders and sintered bulks. The microstructure and chemical composition of sintered bulks were analyzed by electron probe microanalysis using a field emission gun (FE-EPMA) and scanning electron microscopy (SEM) coupled with electron backscatter diffraction (EBSD; Oxford NordlysNano). The grain size in the sample was estimated using the software equipped in the EBSD apparatus. The sintered pellet fabricated by SPS was sliced perpendicularly to the uniaxial pressure direction, rectangular bars were prepared, and the thermoelectric properties were measured. We confirmed that the thermoelectric properties were independent of the cutting direction of the bars, although the crystal structure of BiCuSeO is anisotropic. The electrical resistivity $\rho(T)$ and the Seebeck coefficient $S(T)$ were simultaneously measured at the temperature range from 300 to 973 K using an automated measuring system (Ozawa Science RZ2001i) and the thermoelectric power factor $P = S^2/\rho$ was calculated. The thermal conductivity $\kappa(T)$ was measured in vacuum by a laser flash method (Ulvac-Riko TC-7000) from 300 to 873 K. To examine the accuracy of $\kappa(T)$, we also estimated $\kappa(T)$ using the relation $\kappa = D\alpha C$, where α is the thermal diffusivity, which was measured by a laser flash method, C is the specific heat, which was measured by differential scanning calorimetry (DSC), and D is the mass density, which was measured by the Archimedes method. The difference in $\kappa(T)$ between the two methods was estimated to be about 20%. The $\rho(T)$ and $\kappa(T)$ below 300 K were also measured by a conventional four-terminal method and a steady-state heat flow method, respectively, using a home-made measuring system.[28] The dimensionless figure of merit, $ZT = S^2T/\rho\kappa$, was estimated using the obtained values, in which the involved uncertainty is about 20%.

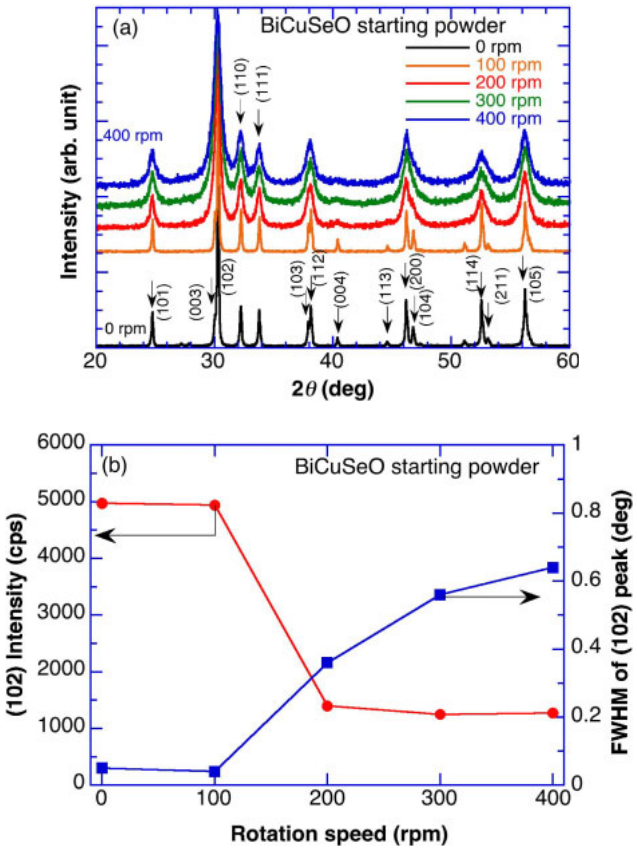

Fig. 1. (Color online) (a) Normalized XRD patterns and (b) (102) peak intensity of the BiCuSeO starting powders, which were ball-milled at various rotation speeds (R). In (b), the FWHM of the (102) peak of the powders is also shown in the right ordinates.

3. Results and discussion

Figures 1(a) and 1(b) show the normalized XRD patterns and (102) peak intensity of the BiCuSeO ($x = 0$) starting powders, respectively, which were ball-milled at various rotation speeds (R). The full width at half maximum (FWHM) of the (102) peak for the powders is also shown in the right ordinates of Fig. 1(b). The XRD pattern of the $R = 100$ rpm powder is nearly identical to that of the $R = 0$ rpm powder, but that of the $R = 200$ rpm powder became fairly broadened and the XRD intensity also decreased. The FWHM of the (102) peak suddenly increased for the $R = 200$ rpm powder and increased gradually with increasing R. For the $R = 300$ and 400 rpm powders, the width and intensity of the diffraction peak changed moderately. These ball-milling effects can be seen usually, during the decrease in crystallite size and the creation of the amorphous phase. No impurity phase was detected by the XRD measurements.

Figure 2 shows EBSD images of the BiCuSeO bulks sintered by SPS using powders of $R = 0$, 200, and 400 rpm. The crystal grains were randomly oriented and the grain size decreased with increasing R. Note that there are many elongated crystals in the $R = 400$ rpm sintered bulk as shown in Fig. 2(c), which were also reported in a previous paper.[24]

Figures 3(a) and 3(b) present the crystallite size of the $Bi_{1-x}Sr_xCuSeO$ starting powders ($x = 0, 0.1$) estimated using the Scherrer equation and the grain size in the sintered pellets

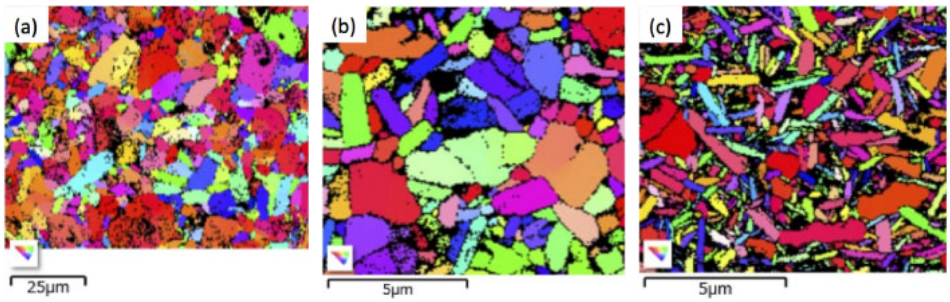

Fig. 2. (Color online) EBSD images of the BiCuSeO sintered bulks fabricated using powders at (a) $R = 0$ rpm, (b) $R = 200$ rpm, and (c) $R = 400$ rpm.

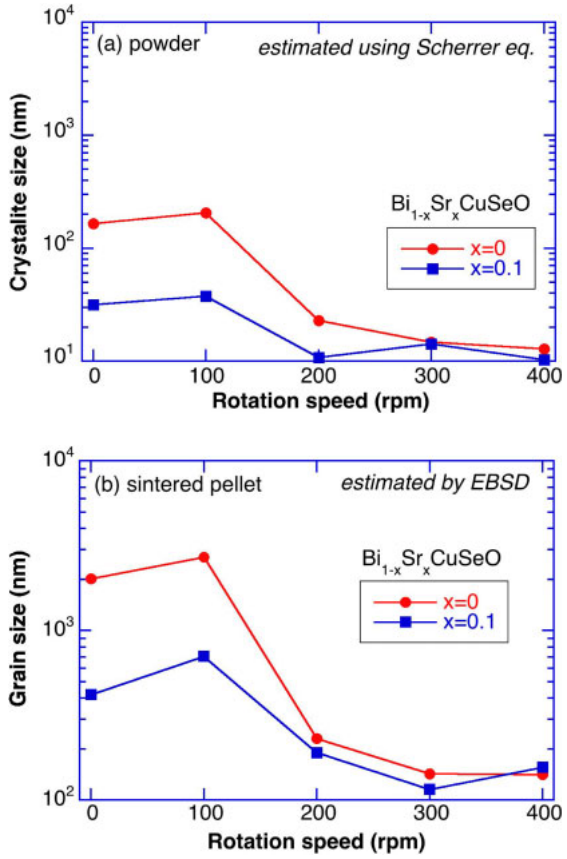

Fig. 3. (Color online) (a) Crystallite size of the $Bi_{1-x}Sr_xCuSeO$ ($x = 0, 0.1$) starting powders estimated using Scherrer equation and (b) grain size in the sintered pellets estimated by EBSD observation, as a function of the rotation speed R.

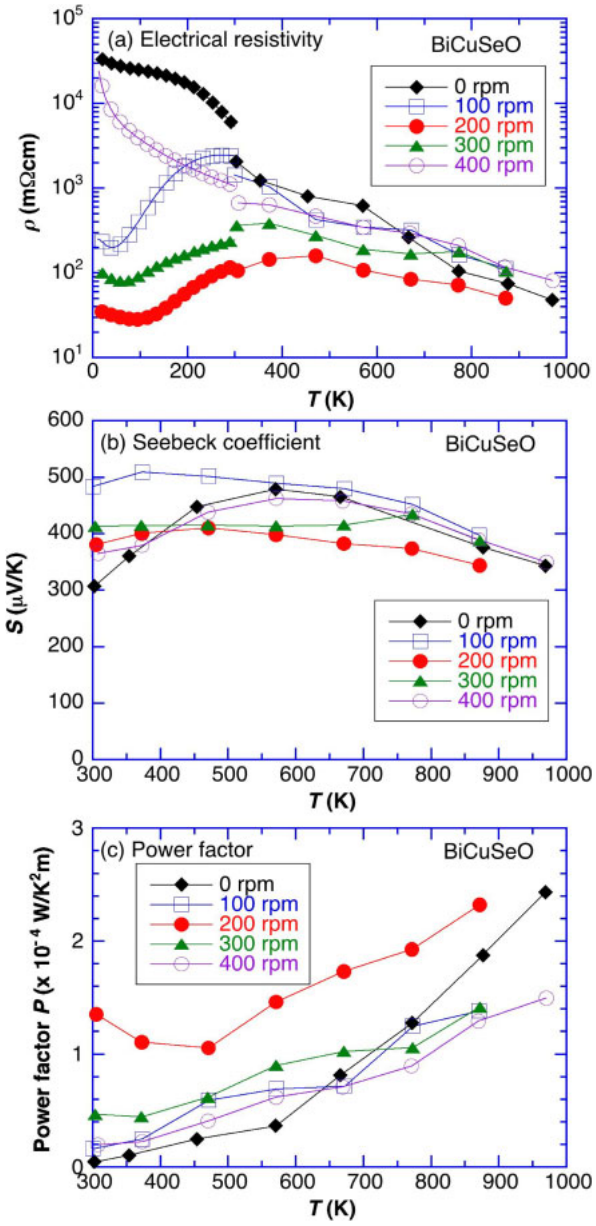

Fig. 4. (Color online) Temperature dependences of the (a) electrical resistivity $\rho(T)$, (b) Seebeck coefficient $S(T)$, and (c) thermoelectric power factor $P(T)$ of the BiCuSeO bulk samples fabricated using starting powders at various rotation speeds (R).

estimated by EBSD observation, respectively, as a function of the rotation speed R. In Fig. 3(a), the crystallite size of the starting powders decreases with increasing R and a steplike decrease can be clearly observed at $R = 200$ rpm, which is consistent with the results in Fig. 1(b). The crystallite size of the $x = 0.1$ series is smaller than that of the $x = 0$ series, which originates from the suppression of the grain growth due to the Sr substitution during the precursor synthesis in the sealed tube. After the subsequent SPS process, the grain size of the bulk samples becomes about one order of magnitude larger than the crystallite size of the starting powders due to the grain growth. However, the sintered bulk samples took over the trend of the starting powders; the grain size estimated by EBSD suddenly decreased at $R = 200$ rpm for both series. The decrease in grain size induces the increase in the number of grain boundaries and, as a result, is expected to decrease the thermal conductivity. The existence of the characteristic rotation speed and milling time is also reported in other papers.[25,26)]

Figure 4 shows the temperature dependences of the electrical resistivity $\rho(T)$, the Seebeck coefficient $S(T)$, and

the thermoelectric power factor $P(T)$ of the BiCuSeO sintered bulks fabricated using starting powders of various rotation speeds (R). In Fig. 4(a), low-temperature ($T < 300$ K) $\rho(T)$ values are also shown, in which a slight discontinuity can be seen around 300 K from the results obtained using different measuring apparatuses above and below 300 K. The high temperature $\rho(T)$ ($T > 300$ K) of all the samples presents a semiconducting behavior of $\rho(T)$ decreasing with increasing T. The ρ of the bulk without ball milling ($R = 0$ rpm) is the highest, but ρ is minimum for the $R = 200$ rpm sample and then increases with R. On the other hand, at $T < 300$ K, the $\rho(T)$ values of the $R = 0$ and 400 rpm samples show a semiconducting behavior, but those of the $R = 200$ and 300 rpm bulk samples show a rather metallic behavior. Since the low-temperature $\rho(T)$ reflects sensitively the number of carriers, these results suggest that the carriers were effectively created during the ball milling process under the rotation speed from 100 to 300 rpm. The increased number of acceptor-like crystal defects was produced via broken layered structures through mechanical stress during the ball milling process.

In Fig. 4(b), the $S(T)$ value of the $R = 200$ rpm sample is the lowest at $T > 473$ K and, roughly, all the $S(T)$ values decrease with increasing T at higher temperatures. Since the Seebeck coefficient is inversely proportional to log n (n: carrier concentration) in a classical wide-gap semiconductor model, the reduced $S(T)$ value might be caused by the enhanced carrier concentration, and the $\rho(T)$ and $S(T)$ values are closely related to each other. The thermoelectric power factor $P(T)$ ($= S^2/\rho$), as shown in Fig. 4(c), increases with T, and that of the $R = 200$ rpm sample is the highest, which results from both the lowest $\rho(T)$ and not so small $S(T)$ values.

We consider the reason why the ρ values of the BiCuSeO samples decrease during the ball milling process. If the stoichiometry of the BiCuSeO compound is ideally realized, in which $[Cu_2Se_2]^{2-}$ and $[Bi_2O_2]^{2+}$ layers are alternately stacked, there are no mobile carriers and then $\rho(T)$ becomes fairly large and $S(T)$ also shows either a large positive or negative value. However, the present BiCuSeO bulk samples showed p-type conductivity owing to the introduction of a very small number of hole carriers, which may originate from the nonstoichiometry of the constituent elements. If a lower level of Cu deficiency is introduced to the nondoped BiCuSeO powder during ball milling, hole carriers are created as shown by the following defect equation:[23)]

$$2BiCu_{1-x}SeO = [Bi_2O_2]^{2+} + [Cu_{2(1-x)}Se_2]^{(2+x)-} + xV_{Cu}^{-} + 2xh^{+}. \quad (1)$$

If Bi deficiency is introduced into the BiCuSeO crystal, hole carriers are also created as shown by the following defect equation:

$$2Bi_{1-x}CuSeO = [Bi_{2(1-x)}O_2]^{(2-x)+} + [Cu_2Se_2]^{2-} + xV_{Bi}^{-} + 2xh^{+}. \quad (2)$$

On the other hand, in the cases of Se and O deficiencies during ball milling, which are easy to create because of high vapor pressure, electron carriers should be created from the viewpoint of electrical neutrality.

The results shown in Figs. 4(a) and 4(b) simply suggest that not the electrons but the holes increased in number in the powders during ball milling. If electron carriers are created during ball milling mainly owing to the Se and O deficiencies, intrinsic holes might be compensated by doped electrons. As a result, $\rho(T)$ and $S(T)$ might be increased. The possibility that the Cu and/or Bi elements are preferentially depleted during ball milling is an open question. The depletion of $[Bi_2O_2]^{2+}$ layers during ball milling may also introduce hole carriers into the conductive $[Cu_2Se_2]^{2-}$ layers. We think that hole carriers are created by the crystal defects or imperfections on the grain surface. Small amounts of other impurity phases, which were not detected by XRD measurements, may be introduced to the ball-milled powders and act as mobile holes. The applied energy during the milling process increases proportionally to the square of the rotation speed, R^2, and the shock frequency increases with the number of balls and the rotation speed R.[25)] Although the saturation trend for $R > 200$ rpm can be seen for the crystallite size of the starting powders and the grain size in the bulk samples, thermoelectric properties change intricately depending on the number and species of mobile carriers through the rotation speed R.

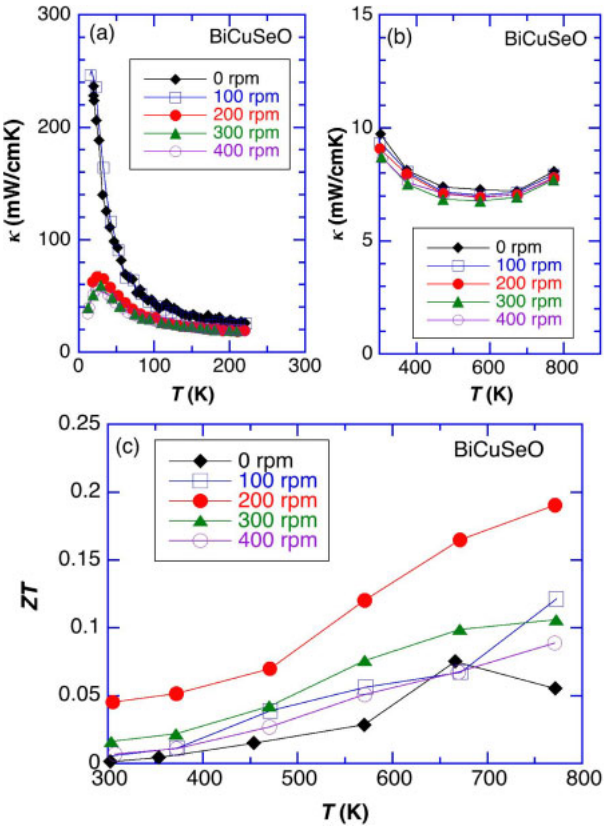

Fig. 5. (Color online) Temperature dependences of the thermal conductivity $\kappa(T)$ values of the BiCuSeO bulk samples fabricated using starting powders at various rotation speeds (R) at (a) $T < 230$ K and (b) $T > 300$ K. (c) Temperature dependence of the thermoelectric figure of merit, $ZT(T)$, of the BiCuSeO bulk samples.

Figures 5(a) and 5(b) show the temperature dependences of the thermal conductivity $\kappa(T)$ values of the BiCuSeO bulk samples at $T < 230$ K and $T > 300$ K, respectively. In Fig. 5(a), a large and sharp $\kappa(T)$ peak is seen at low temperatures for the $R = 0$ and 100 rpm samples; $\kappa(T)$ must be zero at $T = 0$ K, although we cannot confirm the $\kappa(T)$ peak experimentally. However, the $\kappa(T)$ of the samples of $R > 200$ rpm sharply decreased with a broad peak owing to

the increase in crystal defect density. Since the electronic thermal conductivity κ_e, which was estimated on the basis of the Wiedemann–Franz law, was negligibly small, the heat transport was performed entirely by phonons. These results suggest that the $R = 0$ and 100 rpm samples are relatively clean for phonon transport, and that phonon–phonon scattering, which is inversely proportional to temperature, is dominant. However, the phonon scattering due to the crystal defects introduced by ball milling increases for the $R > 200$ rpm samples. In Fig. 5(b), $\kappa(T)$ at $T > 300$ K hardly depends on the rotation speed R at higher temperatures. This result originates from the dominant phonon scattering due to the intrinsic lattice vibration at high temperatures. Figure 5(c) shows the temperature dependence of the thermoelectric figure of merit, $ZT(T)$. The ZT values of all the samples increase with increasing temperature. $ZT(T)$ is maximum for the $R = 200$ rpm sample and then decreases with increasing rotation speed R, which closely reflects the thermoelectric power factor $P(T)$. Because $\kappa(T)$ hardly depends on the rotation speed R at higher temperatures, the maximum ZT of 0.20 was achieved at 773 K for the nondoped BiCuSeO bulk fabricated using the $R = 200$ rpm powder.

Next, we consider the ball milling effect for the Sr-doped $Bi_{1-x}Sr_xCuSeO$ samples ($x = 0.1$). Figure 6 shows the temperature dependences of the electrical resistivity $\rho(T)$, the Seebeck coefficient $S(T)$, and the thermoelectric power factor $P(T)$ of the $Bi_{1-x}Sr_xCuSeO$ samples ($x = 0.1$) using starting powders fabricated at various rotation speeds R. The $\rho(T)$ values of all the samples present a metallic behavior. The ρ of the $R = 0$ rpm bulk is the lowest and increases with R at low temperatures. On the other hand, the $\rho(T)$ at $T > 300$ K seems to be independent of R. These results suggest that the charge carriers were mainly created by the Sr substitution and that the crystal defects introduced by ball milling reduced the electrical conductivity at low temperatures, which is in clear contrast to that observed in the nondoped BiCuSeO samples shown in Fig. 4. In Fig. 6(b), the $S(T)$ values of all the samples increase with increasing T and the $S(T)$ of the $R = 200$ rpm sample is the largest. The $P(T)$ value, as shown in Fig. 6(c), increases with T, and that of the $R = 200$ rpm sample is the highest, which results from larger $S(T)$ values in the samples.

Figures 7(a) and 7(b) show the temperature dependences of the thermal conductivity $\kappa(T)$ values of the $Bi_{1-x}Sr_xCuSeO$ bulk samples ($x = 0.1$) at $T < 230$ K and $T > 300$ K, respectively. In Fig. 7(a), a small $\kappa(T)$ peak can be seen at low temperatures for the $R = 0$ and 100 rpm samples. However, the $\kappa(T)$ peak of the $R > 200$ rpm samples disappeared and the absolute $\kappa(T)$ value decreased. As shown in Fig. 7(b), $\kappa(T)$ at $T > 300$ K slightly decreased with increasing rotation speed R. Figure 7(c) shows the temperature dependence of the thermoelectric figure of merit, $ZT(T)$, of the $Bi_{1-x}Sr_x$-CuSeO bulk samples ($x = 0.1$). The ZT values of all the samples increased with increasing temperature. The $ZT(T)$ value became maximum for the $R = 200$ rpm bulk and then decreased with increasing rotation speed R, which reflected closely the thermoelectric power factor $P(T)$. Because $\kappa(T)$ slightly decreased with the increase in R at higher temperatures, the maximum ZT of 0.46 was achieved at 773 K for the $Bi_{1-x}Sr_xCuSeO$ bulk ($x = 0.1$) fabricated using the $R = 200$ rpm powder.

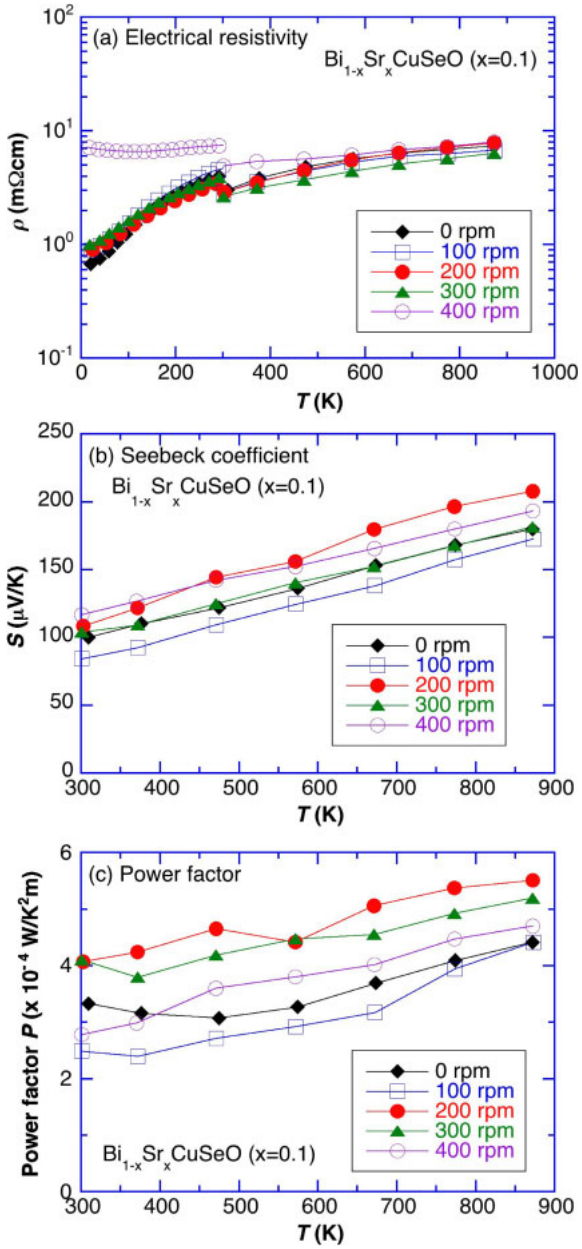

Fig. 6. (Color online) Temperature dependences of the (a) electrical resistivity $\rho(T)$, (b) Seebeck coefficient $S(T)$, and (c) thermoelectric power factor $P(T)$ of the $Bi_{1-x}Sr_xCuSeO$ bulk samples ($x = 0.1$) fabricated using starting powders at various rotation speeds (R).

Figures 8(a) and 8(b) show the electrical resistivity ρ and the Seebeck coefficient S at 773 K for the $Bi_{1-x}Sr_xCuSeO$ samples ($x = 0.1$) fabricated using starting powders at various rotation speeds (R), compared with those for the $x = 0$ bulk samples. The ρ values at 773 K for the $x = 0.1$ samples are about one order of magnitude smaller than those for the $x = 0$ samples owing to the carrier doping, and the S values at 773 K for the $x = 0.1$ samples are about 50% smaller than those for the $x = 0$ samples. Although the R dependences of the ρ and S values of the $x = 0.1$ series are relatively small, a small local maximum of the S value can be seen for $R = 200$ rpm. Figure 8(c) presents the R dependence of the thermoelectric power factor P at 773 K for the $x = 0$ and 0.1 series. The P value for the $x = 0.1$ series is three to four times larger than that for the $x = 0$ series, and the maximum P value can be obtained for the $R = 200$ rpm bulk for both series. The

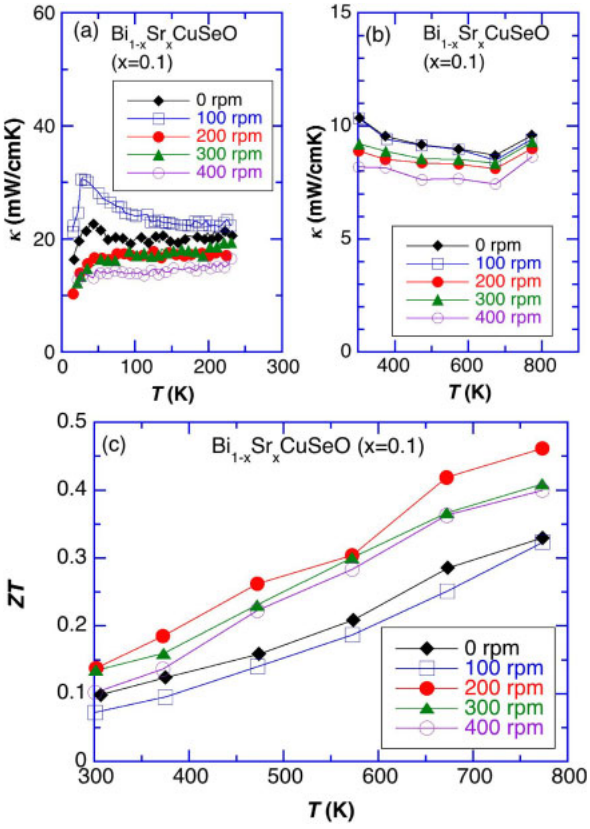

Fig. 7. (Color online) Temperature dependences of the thermal conductivity $\kappa(T)$ values of the $Bi_{1-x}Sr_xCuSeO$ bulk samples ($x = 0.1$) fabricated using starting powders at various rotation speeds (R) at (a) $T < 230$ K and (b) $T > 300$ K. (c) Temperature dependence of the thermoelectric figure of merit, $ZT(T)$, of the $Bi_{1-x}Sr_xCuSeO$ bulk samples ($x = 0.1$).

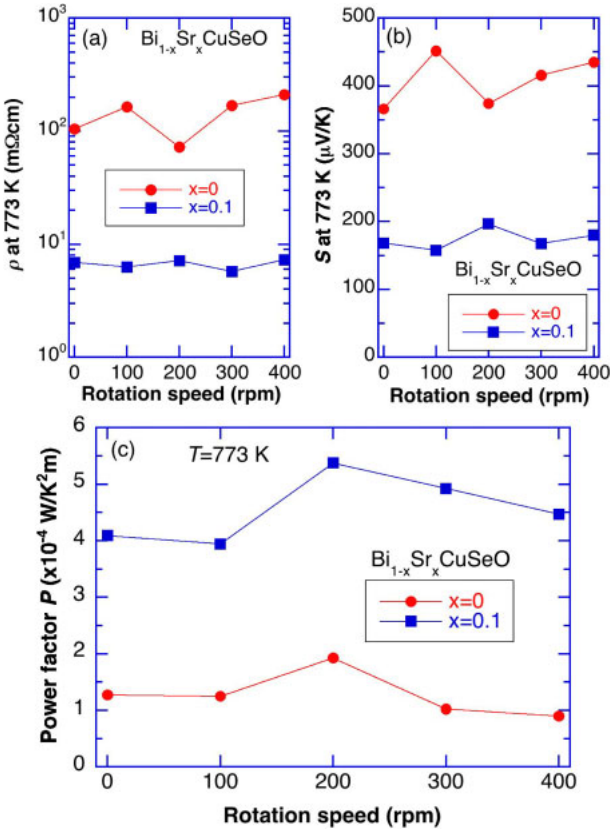

Fig. 8. (Color online) (a) Electrical resistivity ρ, (b) Seebeck coefficient S, and (c) power factor P at 773 K for the $Bi_{1-x}Sr_xCuSeO$ bulk samples ($x = 0, 0.1$) fabricated using starting powders at various rotation speeds (R).

maximum P value of $5.5 \times 10^{-4}\,W\,K^{-2}\,m^{-1}$ was achieved at 773 K for the $Bi_{1-x}Sr_xCuSeO$ bulk ($x = 0.1$) fabricated using the $R = 200$ rpm powder.

Figure 9(a) shows the total thermal conductivity κ, which was measured by a laser flash method, and the electronic thermal conductivity κ_e at 773 K, which was estimated on the basis of the Wiedemann–Franz law, for the $x = 0$ and 0.1 series, as a function of the rotation speed, R. The κ of the $x = 0.1$ series, which is the sum of κ_e and the lattice thermal conductivity $\kappa_{lattice}$ ($\kappa = \kappa_e + \kappa_{lattice}$), is larger than that of the $x = 0$ series, which results from the large contribution of κ_e for the $x = 0.1$ series; about 30% of κ is κ_e. κ slightly decreased with increasing R. Figure 9(b) presents the ZT value at 773 K for the $x = 0$ and 0.1 series as a function of R. The ZT for the $x = 0.1$ series is about two to three times larger than that for the $x = 0$ series, which results mainly from the reduction in thermal conductivity κ, and from the increase in P. The maximum ZT can also be obtained for the $R = 200$ rpm bulks for the $x = 0.1$ series. The maximum ZT value of 0.46 was achieved at 773 K for the $Bi_{1-x}Sr_xCuSeO$ bulk ($x = 0.1$) fabricated using the $R = 200$ rpm powder.

4. Conclusions

We have investigated the ball milling effects for the starting powders of $Bi_{1-x}Sr_xCuSeO$ ($x = 0, 0.1$) on the thermoelectric properties of the subsequent sintered bulks by SPS. The important results and conclusions obtained from this study are summarized as follows.

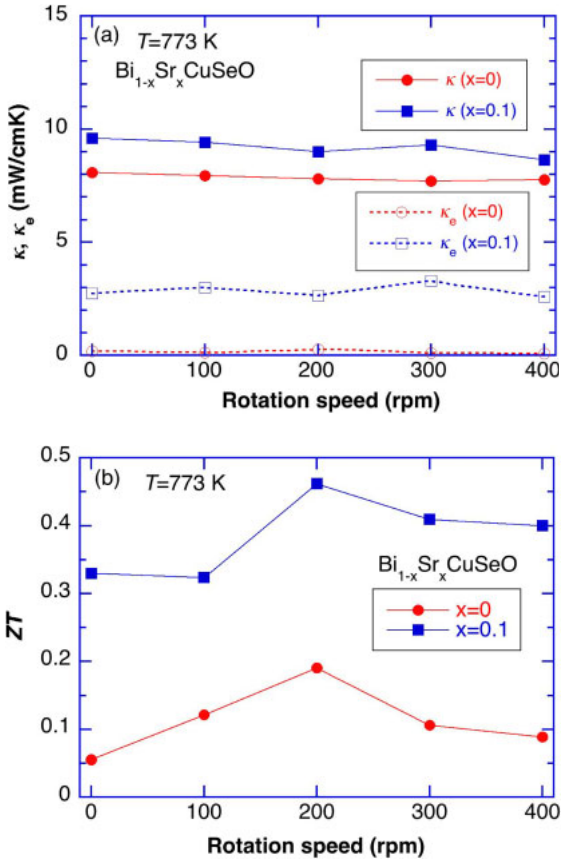

Fig. 9. (Color online) (a) Total thermal conductivity κ and the electronic thermal conductivity κ_e at 773 K for the $x = 0$ and 0.1 series as a function of the rotation speed R. (b) ZT values at 773 K for the $x = 0$ and 0.1 series as a function of R.

1) The crystallite size of ball-milled $Bi_{1-x}Sr_xCuSeO$ powders decreased suddenly at the characteristic rotation speed of $R = 200$ rpm and then gradually with increasing R. The grain size of the $Bi_{1-x}Sr_xCuSeO$ bulks also showed the same tendency, depending on the crystallite size of the starting powders.

2) For the $Bi_{1-x}Sr_xCuSeO$ ($x = 0$) material, the electrical resistivity $\rho(T)$ and the thermal conductivity $\kappa(T)$ changed depending on the rotation speed for the starting powders at $T < 300$ K; mobile carriers were created during the ball milling process, and $\rho(T)$ showed a metallic behavior. The $\kappa(T)$ peak was observed for the $R = 0$ and 100 rpm bulks, but was suppressed for the $R > 200$ rpm bulks owing to the introduction of crystal defects. At $T > 300$ K, the $\rho(T)$ of the $R = 200$ rpm bulk was the lowest, and the Seebeck coefficient $S(T)$ did not decrease. As a result, the power factor $P(T)$ of the $R = 200$ rpm bulk was the largest. The $\kappa(T)$ of the bulks hardly depended on the rotation speed of the starting powders, suggesting that the phonon scattering mainly originates from the lattice vibration.

3) For the $Bi_{1-x}Sr_xCuSeO$ ($x = 0.1$) material, $\rho(T)$ decreased with carrier doping by Sr^{2+} substitution for the Bi^{3+} site and the $P(T)$ value was three to four times larger than that for the $x = 0$ series. $\kappa(T)$ was slightly larger than that for the $x = 0$ series owing to the increase in the electronic thermal conductivity κ_e. The additional increases in P and the figure of merit, ZT, were confirmed at $R = 200$ rpm owing to the ball milling, similarly to that observed for the $x = 0$ series.

Acknowledgment

This work was performed under the Inter-university Cooperative Research Program of the Institute for Materials Research, Tohoku University.

1) B. Poudel, Q. Hao, Y. Ma, Y. C. Lan, A. Minnich, B. Yu, X. Yan, D. Z. Wang, A. Muto, D. Vashaee, X. Y. Chen, J. M. Liu, M. S. Dresselhaus, G. Chen, and Z. Ren, Science **320**, 634 (2008).
2) A. D. LaLonde, Y. Z. Pei, and G. J. Snyder, Energy Environ. Sci. **4**, 2090 (2011).
3) K. F. Hsu, S. Loo, F. Guo, W. Chen, J. S. Dyck, C. Uher, T. Hogan, E. K. Polychroniadis, and M. G. Kanatzidis, Science **303**, 818 (2004).
4) S. Ohta, T. Nomura, H. Ohta, M. Hirano, H. Hosono, and K. Koumoto, Appl. Phys. Lett. **87**, 092108 (2005).
5) M. Ohtaki, T. Tsubota, K. Eguchi, and H. Arai, J. Appl. Phys. **79**, 1816 (1996).
6) D. Bérardan, E. Guilmeau, A. Maignan, and B. Raveau, Solid State Commun. **146**, 97 (2008).
7) L. Xu, F. Li, and Y. Wang, J. Alloys Compd. **501**, 115 (2010).
8) K. Fujita, T. Mochida, and K. Nakamura, Jpn. J. Appl. Phys. **40**, 4644 (2001).
9) A. M. Kusainova, P. S. Berdonosov, L. G. Akselrud, L. N. Kholodkovskaya, V. A. Dolgikh, and B. A. Popovkin, J. Solid State Chem. **112**, 189 (1994).
10) Y. Kamihara, H. Hiramatsu, M. Hirano, R. Kawamura, H. Yanagi, T. Kamiya, and H. Hosono, J. Am. Chem. Soc. **128**, 10012 (2006).
11) Y. Kamihara, T. Watanabe, M. Hirano, and H. Hosono, J. Am. Chem. Soc. **130**, 3296 (2008).
12) M. Palazzi and S. Jaulmes, Acta Crystallogr., Sect. B **37**, 1337 (1981).
13) P. S. Berdonosov, A. M. Kusainova, L. N. Kholodkovskaya, V. A. Dolgikh, L. G. Akselrud, and B. A. Popovkin, J. Solid State Chem. **118**, 74 (1995).
14) C. Barreteau, D. Bérardan, E. Amzallag, L.-D. Zhao, and N. Dragoe, Chem. Mater. **24**, 3168 (2012).
15) H. Hiramatsu, H. Yanagi, T. Kamiya, K. Ueda, M. Hirano, and H. Hosono, Chem. Mater. **20**, 326 (2008).
16) L.-D. Zhao, D. Berardan, Y. L. Pei, C. Byl, L. Pinsard-Gaudart, and N. Dragoe, Appl. Phys. Lett. **97**, 092118 (2010).
17) J. Li, J. Sui, Y. Pei, C. Barreteau, D. Berardan, N. Dragoe, W. Cai, J. He, and L.-D. Zhao, Energy Environ. Sci. **5**, 8543 (2012).
18) J. P. Heremans, V. Jovovic, E. S. Toberer, A. Saramat, K. Kurosaki, A. Charoenphakdee, S. Yamanaka, and G. J. Snyder, Science **321**, 554 (2008).
19) T. C. Harman, P. J. Taylor, M. P. Walsh, and B. E. LaForge, Science **297**, 2229 (2002).
20) J. P. Heremans, C. M. Thrush, and D. T. Morelli, Phys. Rev. B **70**, 115334 (2004).
21) Y.-L. Pei, J. He, J.-F. Li, F. Li, Q. Liu, W. Pan, C. Barreteau, D. Berardan, N. Dragoe, and L.-D. Zhao, NPG Asia Mater. **5**, e47 (2013).
22) L. Pan, D. Bérardan, L. Zhao, C. Barreteau, and N. Dragoe, Appl. Phys. Lett. **102**, 023902 (2013).
23) Y. Liu, L.-D. Zhao, II, Y. Liu, J. Lan, W. Xu, F. Li, B.-P. Zhang, D. Berardan, II, N. Dragoe, II, Y.-H. Lin, C.-W. Nan, J.-F. Li, and H. Zhu, J. Am. Chem. Soc. **133**, 20112 (2011).
24) J. Sui, J. Li, J. He, Y.-L. Pei, D. Berardan, H. Wu, N. Dragoe, W. Cai, and L.-D. Zhao, Energy Environ. Sci. **6**, 2916 (2013).
25) F. Li, J.-F. Li, L.-D. Zhao, K. Xiang, Y. Liu, B.-P. Zhang, Y.-H. Lin, C.-W. Nan, and H.-M. Zhu, Energy Environ. Sci. **5**, 7188 (2012).
26) V. Pele, C. Barreteau, D. Berardan, L. Zhao, and N. Dragoe, J. Solid State Chem. **203**, 187 (2013).
27) P. Scherrer, Göttinger Nachr. Ges. **2**, 98 (1918) [in German].
28) H. Fujishiro, M. Ikebe, T. Naito, K. Noto, S. Kobayashi, and S. Yoshizawa, Jpn. J. Appl. Phys. **33**, 4965 (1994).